# Improved Detectability of Hyper-Dense Nodules with Dual-Energy CT Scans:

# Phantom Study Using Simulated Liver Harboring Nodules

Enkhjargal BAYASGALAN, Toru HIGAKI, Wataru FUKUMOTO, Yuko NAKAMURA,

Keigo CHOSA, Fuminari TATSUGAMI, Yasutaka BABA, Kazuo AWAI*)

Department of Diagnostic Radiology, Graduate School of Biomedical and Health

Sciences, Hiroshima University, Hiroshima, Japan;

1-2-3 Kasumi, Minami-ku, Hiroshima city, 734-8551, Japan

Corresponding author: Kazuo Awai

Email: awai@hiroshima-u.ac.jp

Running title: Detection of hyper-dense nodules on dual-energy CT scan

Key words: liver tumor, hyper-dense nodule, dual-energy CT, Phantom

**ABSTRACT**

The purpose of this study was to investigate whether dual energy CT (DECT) improves the detectability of hyper-dense nodules in a phantom study. We subjected small, medium, and large liver-simulating phantoms harboring simulated hypervascular tumors to arterial-phase hepatic dynamic CT. We obtained 150 single-energy CT (SECT) - and 150 DECT scans and measured the contrast to noise ratio (CNR) of the nodules. The alternative free response receiver observer characteristic (AFROC) curves of 5 radiologists reading the SECT and DECT scans were compared to assess the detectability of hyper-dense nodules. For all phantoms, the CNR of nodules measured with DECT were significantly higher than those with SECT (all $p<0.001$). In the AFROC study, the area under the curve was significantly larger with DECT than SECT (0.778 vs 0.499, $p = 0.012$). On DECT scans, the detectability of high-density nodules was better than on SECT scans.

## INTRODUCTION

The patient body size and cardiac function, the iodine mass of the contrast medium (CM) and its injection rate, and the tube voltage and beam hardening artifacts affect arterial enhancement at computed tomography (CT) (3, 20) . Beam hardening is a physical phenomenon that may affect organ enhancement on contrast-enhanced CT scans (5, 24) . Schindera et al. performed *in vivo* and *in vitro* single energy CT (SECT) studies reported that beam hardening reduced the degree of arterial enhancement in large-bodied patients undergoing CT angiography (20). Decreasing arterial enhancement by beam hardening may impair identification or characterization of lesions which shows arterial enhancement at CT.

Hepatic hypervascular lesions are defined as lesions whose attenuation is higher than in the surrounding liver parenchyma during arterial-phase dynamic CT(2). Their identification and characterization is of diagnostic importance and necessary for the selection of appropriate treatment strategies (4, 7, 13). In large-scale patients, the intensity of hypervascular liver lesions may be decreased due to beam hardening.

Recently clinically induced dual energy CT (DECT) can reduce beam hardening artifact.(16, 25) We hypothesized that conspicuity of hypervascular lesions was decreased due to beam hardening on SECT and DECT could reduce beam hardening

artifacts and improve lesion conspicuity. The purpose of this study was to investigate whether DECT could improve detectability of hyper-dense nodule in a phantom study.

## MATERIALS AND METHODS

Our phantoms simulating liver harboring simulated hypervascular tumors during the arterial phase at hepatic dynamic CT were prepared using a three-dimensional (3D) printer (Agilista 3200, Keyence, Osaka, Japan) (Figs 1A-C). The central body of the phantoms was made of acrylate plastic whose CT number was approximately 60 HU when measured on 120 kVp SECT images. The size of the central body was 300 x 200 mm in the axial plane (xy-direction), 50 mm along the z axis (Fig. 1A); it harbored 102 spherical holes (10-mm diameter). A 3-mm-diameter columnar path connected the holes with the phantom's exterior (Fig 1B). To simulate hyper-dense nodules, we used the paths to inject a solution containing iodine contrast medium (CM; Omnipaque-300, Daiichi-Sankyo, Tokyo, Japan) into 1 - 3 arbitrarily chosen spherical holes. The CT number of the nodules was adjusted to be 10 HU higher than the CT number of the phantom body when measured on 120 kVp SECT images. Iodine concentration of iodine solution was 300 mg/mL. We filled the remaining holes with a sugar solution; their CT number was adjusted to be the same as the CT number of the phantom body.

The central body was designated as the small phantom. To create the medium-size phantom, we surrounded the central body with a 15-mm wide, 350 x 250 mm outer diameter frame; the large phantom was encompassed by a 15-mm-wide, 400 x 300 mm

outer diameter frame. Both frames were made of the same material as the central body (Fig 1A).

CM was injected via the paths into 1- 3 arbitrarily-chosen holes in the central body to mimic hyper-dense nodules; 4 bodies harbored one-, 12 featured 2, and 14 contained 3 nodules (30 bodies, 70 nodules)**.** Another 20 bodies were free of nodules. We subjected each phantom (small, medium, large) to SECT and DECT scanning.

**CT scanning and Image reconstruction**

The phantoms were scanned using a 320-detector row CT scanner (Aquilion ONE ViSION Ed., Canon Medical Systems, Otawara, Japan). We acquired SECT scans at 120 kVp. DECT scans were performed first at 80- and then at 135kVp. We applied the volume scan mode (axial non-helical scan mode); the detector configuration for all scans was 80 x 0.5mm.

For SECT scans of the small phantom, the tube current was 85 mAs (170 mA and 0.5 sec/rotation), for medium phantoms the settings were 175 mAs (350 mA and 0.5 sec/rotation), and for large phantoms they were 250 mAs (250 mA and 1.0 sec/rotation). The $CTDI_{vol}$ for small, medium, and large phantoms was 8.2, 16.9, and 23.7 mGy, respectively.  Preset image noise index was 12 in all phantoms.

For DECT scans of the small phantom we set the the tube current second to be almost the same $CTDI_{vol}$ as for the SECT scans, i.e. 145 mAs at 80 kVp (290 mA and 0.5 sec/rotation) and 25 mAs at 135 kVp (50 mA and 0.5 sec/rotation). For medium phantoms the settings were 315 mAs at 80 kVp (630 mA and 0.5 sec/rotation) and 55 mAs at 135 kVp (110 mA and 0.5 sec/rotation); for large phantoms they were 460 mAs at 80 kVp (460 mA and 1.0 sec/rotation) and 80 mAs at 135 kVp (80 mA and 1.0 sec/rotation). The $CTDI_{vol}$ of DECT scans for small, medium, and large phantoms was 8.0, 17.6, and 25.0 mGy, respectively.

From DECT scans we generated virtual monochromatic 65 keV CT (VMCT) images corresponding to 120 kVp SECT images. Although our CT system can generate both image-based and projection-based VMCT images, (25) we produced projection-based VMCT images. We reconstructed both scan data with hybrid iterative reconstruction [adaptive iterative dose reduction 3D (AIDR-3D), Canon Medical Systems] with reconstruction kernel FC13, the standard kernel for abdominal CT.

**Quantitative analysis of the phantom images**

One radiologist with 4 years of experience with body CT imaging determined the CT number of the 70 hyper-dense nodules on SECT and DECT images. The CT number

and its standard deviation [SD] at 4 sites around each nodule were also recorded. An attempt was made to maintain a constant region of interest (ROI) of approximately 50 $mm^2$. The mean CT number of the 4 sites was considered to be the background CT number of the phantom and the mean of the SD of those sites as the image noise. The contrast-to-noise ratio (CNR) of each nodule was calculated with the formula: CNR = [(CT number of the nodule)-(CT number of background)]/image noise. Measurements were performed using Image J (https://imagej.nih.gov/ij/download.html). We used a gray-scale monitor (Model PA301A; NEC, Tokyo, Japan) with a spatial resolution of 2560 x 1600 for quantitative analysis.

**Observer performance study**

Five board-certified radiologists with 8 - 31 years of experience with body CT imaging (median 17 years) participated in the observer performance study; the software used in the study was developed by one of the authors (TH). The 5 radiologists were trained on 12 images (9 with- and 3 without nodules) to make sure they could operate the observer interface. No training images were included in the observer performance study.

The readers were presented with a total of 300 images to be read in one session [images of 30 phantoms with- plus 20 without nodules (50 images) x 2 modalities (SECT

and DECT) x 3 (small, medium, large phantoms) = 300 total images]. Of the phantoms, 4 harbored one-, 12 featured 2, and 14 contained 3 nodules (30 phantoms 70 nodules); 20 images were free of nodules. The observers first marked the location of hyper-dense nodules on each image by clicking a mouse. They then rated their confidence in their identification of the nodule(s) on the right side of the screen (Rating score, 100: definitely identified; 0: definitely not identified). The images were presented in random order. The window level and screen width could be set freely. No restrictions were placed on the reading time; each reading session required approximately 2 hours. We used the same gray-scale monitor as in our quantitative analysis of observer performance.

**Statistical analysis**

All numerical data are presented as the median and the range. We used the Wilcoxon signed-rank test and Medcalc version 18 (Medcalc Software bvba, Ostend, Belgium) to compare the contrast and the CNR on DECT and SECT images obtained for small, medium, and large phantoms. Jackknife alternative free-response ROC (JAFROC) analysis was performed to compare observer performance for detecting hyper-density nodules on images obtained by DECT and SECT. The multiple-reader multiple-case (MRMC) design for JAFROC analysis takes into account the tumor location and allows

the evaluation of multiple lesions on each image To analyze MRMC-JAFROC data we employed DBM-MRMC Software (6) provided by Chakraborty and Yoon (JAFROC 4.2.1, http://www.devchakraborty.com/index.php). We generated AFROC curves by plotting the lesion localization fraction against the false positive fraction and used the area under the curve (AUC) as the figure of merit (FOM) for the detectability of hyper-dense nodules. We applied statistical tests to all phantom data obtained by SECT and DECT. To avoid statistical errors due to multiple observations we did not perform sub-analyses of findings made on small, medium, and large phantoms(9). Differences of $p < 0.05$ were recorded as statistically significant.

## RESULTS

As shown in Table 1, on SECT and DECT images, the CNR of nodules decreased with the phantom size. The CNR on SECT scans of the large phantoms was 85% lower than on the small phantoms; on DECT images it was 28.7% lower on large- than small phantoms. For all 3 phantoms the CNR of nodules measured with DECT was significantly higher than those with SECT (all: $p<0.001$). (Fig 2).

The AUC values for five observers are shown in Table 2 and their averaged AFROC curves for the detection of hyper-dense nodules on SECT and DECT scans in Fig 3. Standard deviations of AUC values for SECT and DECT were 0.14 and 0.07, respectively and they were relatively small (Table 2). In averaged AFROC curves for all observers, the AUC values obtained with SECT and DECT for the detection of hyper-dense nodules were 0.50 and 0.77, respectively (Fig 3A); the difference was statistically significant ($p = 0.012$). In all of the small, medium, and large phantoms, the AUC values for DECT were larger than that for DECT (Figs 3B - 3D).

Representative phantom images are presented in Figs 4A - 4F**.** With all 3 phantoms, hyper-dense nodules were more clearly demonstrated on DECT than SECT images while the tendency in the large phantom was relatively small.

## DISCUSSION

We found that the CNR of simulated hyper-dense nodules was higher on DECT than SECT images irrespective of the phantom size ($p < 0.001$) and that the AUC values for the detection of such nodules were also significantly higher with DECT than SECT ($p = 0.012$). These findings indicate that DECT was superior to SECT for the detection of simulated hyper-dense nodules in our phantom study.

Beam hardening is a phenomenon in which the mean energy of a polychromatic x-ray increases as it passes through tissue or media. The absorption of lower-energy photons in the spectrum is increased, resulting in less and less attenuation of the beam per unit length(24) . Consequently, the CT number in the inner part of the body is lower than in the outer part, a phenomenon known as the Cupping artifact(5) . The CNR of hyper-dense nodules decreased as the size of our phantoms subjected to SECT or DECT scanning increased, a finding we attribute to the enhancement of beam hardening with the increase in the size of the phantoms.

The CNR decrease as the phantom size increased was less on DECT than SECT images. We generated VMCT images using a projection-based method. The main difference between projection- and image-based VMCT imaging is the method by which the mass density of the two basis materials is determined. For example, in DECT, two basis

materials such as water and iodine are arbitrarily predetermined by radiologists to specify tissue components.

Application of the projection-based method more effectively reduces beam-hardening artifacts because beam hardening occurs in each x-ray projection(25). Theoretically, if the CT x-ray is truly monochromatic, the phantom size has no effect on the CNR because there is no beam hardening effect. However, on our VMCT images generated from DECT data, the CNR did decrease as the phantom size increased. This suggests the post-correction persistence of residual artifacts even on VMCT images and a physical model (spectrum, detector, imaging material) needs to be established(14).

Others (1, 10, 11, 17, 19) who used the CNR or the signal-to-noise ratio (SNR) as the FOM reported that with DECT, the conspicuity of hypervascular tumors or iodine-enhanced lesions could be improved. We, on the other hand, used the CNR and the AUC of the AFROC study to compare SECT and DECT in our observer performance study. As the conspicuity of liver tumors is affected by the tumor-to-liver contrast (2, 8, 23) and the image noise, the CNR has become the index for tumor conspicuity(12, 15, 21, 22). However, the CNR is not always directly correlated with diagnostic capability (12) because the noise frequency also affects lesion conspicuity. Therefore, we think that not only CNR evaluation but also ROC studies must be performed to confirm lesion

detectability in the clinical setting.

Our findings suggest that the detectability of hypervascular liver tumors can be improved by obtaining VMCT images, especially in patients with a larger abdominal circumference. Their acquisition may greatly improve the detection of hypervascular liver tumors not only in obese patients but also in patients with massive ascites frequently encountered in the presence of cirrhosis complicated by hepatocellular carcinoma. Metastatic liver tumors can be also accompanied by massive ascites due to carcinomatous peritonitis, resulting in enlargement of the abdominal circumference that may impair the detection of hypervascular liver tumors.

In this study, we used 10 mm diameter simulated nodules and adjusted their CT number of the nodules to be 10 HU higher than the CT number of the phantom body. Yanaga et al. reported that 95% confidence interval of the tumor–liver contrast in which hypervascular hepatocellular carcinoma is barely demonstrated was 17.3-25 HU in a clinical study (23). As our study was a phantom study and background of the phantom was homogeneous and there may be fewer artifacts than in clinical setting, we adopted 10 HU in difference of CT number between simulated nodules and background. Furthermore, the reason why we adopted nodule diameter of 10 mm was that American College of Radiology LI-RADS

(https://www.acr.org/Clinical-Resources/Reporting-and-Data-Systems/LI-RADS/CT-MRI-LI-RADS-v2017) uses 10 mm as its minimum when characterizing observations for arterial phase hyper-enhancement.

Our study has some limitations. We generated our VMCT images at constant 65 keV from DECT data. Although specific keV values yield the lowest image noise and the highest CNR on different DECT scanners (15, 17, 18, 25), Mileto et al.(19) reported that the optimal monochromatic energy level for maximizing the conspicuity of hypervascular liver tumors was significantly affected by the body habitus. They also found that higher keV levels are optimal for use in the study of large phantoms. From these stand points, selection of different keV according phantom size might be better. Second, the 50-mm thickness of our phantom may have been too thin because the total detector width of the CT scanner was 40 mm at the isocenter of the x-ray. Consequently, scatter x-ray may have affected our results.

In conclusion, when we acquired scans mimicking the hepatic arterial phase of hepatic dynamic CT in our phantom study, DECT was superior to SECT for the detection of hyper-dense nodules simulating hypervascular liver tumors. The findings reported here are preliminary and we are planning to perform clinical studies to confirm our observations.

Summary

We concluded that DECT was superior to SECT for the detection of hyper-dense nodules simulating hypervascular liver tumors from our phantom study. Limitations of our study were that we used VMCT images at constant 65 keV from DECT data and the 50-mm thickness of our phantom in this phantom experiment. We should perform clinical studies to confirm our observations of this phantom study.

## REFERENCES

1. Altenbernd J, Heusner TA, Ringelstein A, Ladd SC, Forsting M, Antoch G. 2011. Dual-energy-CT of hypervascular liver lesions in patients with HCC: investigation of image quality and sensitivity. Eur Radiol. 21:738-743.

2. Awai K, Takada K, Onishi H, Hori S. 2002. Aortic and hepatic enhancement and tumor-to-liver contrast: analysis of the effect of different concentrations of contrast material at multi-detector row helical CT. Radiology. 224:757-763.

3. Bae KT. 2010. Intravenous contrast medium administration and scan timing at CT: considerations and approaches. Radiology. 256:32-61.

4. Baron RL. 1994. Understanding and optimizing use of contrast material for CT of the liver. AJR Am J Roentgenol. 163:323-331.

5. Barrett JF, Keat N. 2004. Artifacts in CT: recognition and avoidance. Radiographics. 24:1679-1691.

6. Dorfman DD, Berbaum KS, Metz CE. 1992. Receiver operating characteristic rating analysis. Generalization to the population of readers and patients with the jackknife method. Invest Radiol. 27:723-731.

7. European Association For The Study Of The L, European Organisation For R, Treatment Of C. 2012. EASL-EORTC clinical practice guidelines: management of

hepatocellular carcinoma. J Hepatol. 56:908-943.

8. Furlan A, Marin D, Vanzulli A, Patera GP, Ronzoni A, Midiri M, et al. 2011. Hepatocellular carcinoma in cirrhotic patients at multidetector CT: hepatic venous phase versus delayed phase for the detection of tumour washout. Br J Radiol. 84:403-412.

9. Gonen M, Panageas KS, Larson SM. 2001. Statistical issues in analysis of diagnostic imaging experiments with multiple observations per patient. Radiology. 221:763-767.

10. Grosse Hokamp N, Hoink AJ, Doerner J, Jordan DW, Pahn G, Persigehl T, et al. 2017. Assessment of arterially hyper-enhancing liver lesions using virtual monoenergetic images from spectral detector CT: phantom and patient experience. Abdom Radiol (NY). Nov 28. [Epub ahead of print]

11. Husarik DB, Gordic S, Desbiolles L, Krauss B, Leschka S, Wildermuth S, et al. 2015. Advanced virtual monoenergetic computed tomography of hyperattenuating and hypoattenuating liver lesions: ex-vivo and patient experience in various body sizes. Invest Radiol. 50:695-702.

12. Jensen K, Andersen HK, Tingberg A, Reisse C, Fosse E, Martinsen AC. 2016. Improved Liver Lesion Conspicuity With Iterative Reconstruction in Computed Tomography Imaging. Curr Probl Diagn Radiol. 45:291-296.

13. Kudo M, Izumi N, Kokudo N, Matsui O, Sakamoto M, Nakashima O, et al. 2011. Management of hepatocellular carcinoma in Japan: Consensus-Based Clinical Practice Guidelines proposed by the Japan Society of Hepatology (JSH) 2010 updated version. Dig Dis.29:339-364.

14. Kyriakou Y, Meyer E, Prell D, Kachelriess M. 2010. Empirical beam hardening correction (EBHC) for CT. Med Phys. 37:5179-5187.

15. Leng S, Yu L, Fletcher JG, McCollough CH. 2015. Maximizing Iodine Contrast-to-Noise Ratios in Abdominal CT Imaging through Use of Energy Domain Noise Reduction and Virtual Monoenergetic Dual-Energy CT. Radiology. 276:562-570.

16. Marin D, Boll DT, Mileto A, Nelson RC. 2014. State of the art: dual-energy CT of the abdomen. Radiology. 271:327-342.

17. Marin D, Ramirez-Giraldo JC, Gupta S, Fu W, Stinnett SS, Mileto A, et al. 2016. Effect of a Noise-Optimized Second-Generation Monoenergetic Algorithm on Image Noise and Conspicuity of Hypervascular Liver Tumors: An In Vitro and In Vivo Study. AJR Am J Roentgenol. 206:1222-1232

18. Matsumoto K, Jinzaki M, Tanami Y, Ueno A, Yamada M, Kuribayashi S. 2011. Virtual monochromatic spectral imaging with fast kilovoltage switching: improved image quality as compared with that obtained with conventional 120-kVp CT. Radiology.

259:257-262.

19. Mileto A, Nelson RC, Samei E, Choudhury KR, Jaffe TA, Wilson JM, et al. 2014. Dual-energy MDCT in hypervascular liver tumors: effect of body size on selection of the optimal monochromatic energy level. AJR Am J Roentgenol. 203:1257-1264.

20. Schindera ST, Tock I, Marin D, Nelson RC, Raupach R, Hagemeister M, et al. 2010. Effect of beam hardening on arterial enhancement in thoracoabdominal CT angiography with increasing patient size: an in vitro and in vivo study. Radiology. 256:528-535.

21. Shuman WP, Green DE, Busey JM, Kolokythas O, Mitsumori LM, Koprowicz KM, et al. 2013. Model-based iterative reconstruction versus adaptive statistical iterative reconstruction and filtered back projection in liver 64-MDCT: focal lesion detection, lesion conspicuity, and image noise. AJR Am J Roentgenol. 200:1071-1076.

22. Shuman WP, Green DE, Busey JM, Mitsumori LM, Choi E, Koprowicz KM, et al. 2014. Dual-energy liver CT: effect of monochromatic imaging on lesion detection, conspicuity, and contrast-to-noise ratio of hypervascular lesions on late arterial phase. AJR Am J Roentgenol. 203:601-606.

23. Yanaga Y, Awai K, Nakaura T, Namimoto T, Oda S, Funama Y, et al. 2008. Optimal contrast dose for depiction of hypervascular hepatocellular carcinoma at dynamic CT using 64-MDCT. AJR Am J Roentgenol. 190:1003-1009.

24. Young SW, Muller HH, Marshall WH. 1983. Computed tomography: beam hardening and environmental density artifact. Radiology. 148:279-283.

25. Yu L, Leng S, McCollough CH. 2012. Dual-energy CT-based monochromatic imaging. AJR Am J Roentgenol. 199 (5 Suppl): S9-S15.

## FIGURE LEGENDS

**Fig 1**. Configuration of the central body of our phantoms.

**A**: The phantom (representing a small phantom) consists of a central body (size in xy dimension, 300 x 200 mm; thickness 50 mm). The phantom size was increased by encompassing the central body with 15-mm-wide frames made of the same material as the central body.

**B**: Detailed structure of the central body of the phantom. The central body harbors 102 spherical holes (10 mm in diameter) to simulate nodules. A 3-mm-diameter columnar path allows for the injection of CM to mimic nodules.

**C**: Photograph of a phantom showing the frames used to increase the phantom size.

**Fig 2.** Comparison of the CNR of hyper-dense nodules on SECT and DECT scans of small, medium, and largesized phantoms. For all phantoms the CNR of nodules was significantly higher on DECT than SECT scans (all, $p<0.001$).

**Fig 3** Averaged alternative free-response ROC curves for all observers tasked with the detection of hyper-dense nodules on SECT and DECT scans.

**A**: All phantoms: Averaged AFROC curves for all observers. The AUC value was

0.50 for SECT and 0.77 for DECT (p = 0.012).

**B**: Small phantom: Averaged AFROC curves for all observers. The AUC value was 0.70 for SECT and 0.84 for DECT.

**C**: Medium phantom: Averaged AFROC curves for all observers. The AUC value was 0.44 for SECT and 0.87 for DECT.

**D**: Large phantom: Averaged AFROC curves for all observers. The AUC value was 0.36 for SECT and 0.63 for DECT**.**

**Fig 4.** CT images of the phantoms.

**A**: SECT: Small phantom.

**B**: SECT: Medium phantom.

**C**: SECT: Large phantom.

**D**: DECT: Small phantom.

**E**: DECT: Medium phantom.

**F**: DECT: Large phantom.

Arrows indicate hyper-dense nodules consisting of a solution of iodine contrast media. With all 3 phantoms, hyper-dense nodules were more clearly demonstrated on DECT than SECT images.

1. Altenbernd, J., Heusner, T.A., Ringelstein, A., Ladd, S.C., Forsting, M. and Antoch, G. Dual-energy-CT of hypervascular liver lesions in patients with HCC: investigation of image quality and sensitivity. Eur Radiol. 2011 Apr;21(4):738-43.
2. Awai, K., Takada, K., Onishi, H. and Hori, S. Aortic and hepatic enhancement and tumor-to-liver contrast: analysis of the effect of different concentrations of contrast material at multi-detector row helical CT. Radiology. 2002 Sep;224(3):757-63.
3. Bae, K.T. Intravenous contrast medium administration and scan timing at CT: considerations and approaches. Radiology. 2010 Jul;256(1):32-61.
4. Baron, R.L. Understanding and optimizing use of contrast material for CT of the liver. AJR Am J Roentgenol. 1994 Aug;163(2):323-31.
5. Barrett, J.F. and Keat, N. Artifacts in CT: recognition and avoidance. Radiographics. 2004 Nov-Dec;24(6):1679-91.
6. Dorfman, D.D., Berbaum, K.S. and Metz, C.E. Receiver operating characteristic rating analysis. Generalization to the population of readers and patients with the jackknife method. Invest Radiol. 1992 Sep;27(9):723-31.
7. European Association For The Study Of The L, European Organisation For R, Treatment Of C. EASL-EORTC clinical practice guidelines: management of hepatocellular carcinoma. J Hepatol. 2012 Apr;56(4):908-43.
8. Furlan, A., Marin, D., Vanzulli, A., Patera, G.P., Ronzoni, A., Midiri, M. et al. Hepatocellular carcinoma in cirrhotic patients at multidetector CT: hepatic venous phase versus delayed phase for the detection of tumour washout. Br J Radiol. 2011 May;84(1001):403-12.
9. Gonen, M., Panageas, K.S. and Larson, S.M. Statistical issues in analysis of diagnostic imaging experiments with multiple observations per patient. Radiology. 2001 Dec;221(3):763-7.
10. Grosse, Hokamp. N., Hoink, A.J., Doerner, J., Jordan, D.W., Pahn, G., Persigehl, T. et al. Assessment of arterially hyper-enhancing liver lesions using virtual monoenergetic images from spectral detector CT: phantom and patient experience. Abdom Radiol (NY). 2017 Nov 28.
11. Husarik, D.B., Gordic, S., Desbiolles, L., Krauss, B., Leschka, S., Wildermuth, S. et al. Advanced virtual monoenergetic computed tomography of hyperattenuating and hypoattenuating liver lesions: ex-vivo and patient experience in various body sizes. Invest Radiol. 2015 Oct;50(10):695-702.
12. Jensen, K., Andersen, H.K., Tingberg, A., Reisse, C., Fosse, E. and Martinsen,

A.C. Improved Liver Lesion Conspicuity With Iterative Reconstruction in Computed Tomography Imaging. Curr Probl Diagn Radiol. 2016 Sep-Oct;45(5):291-6.
13. Kudo, M., Izumi, N., Kokudo, N., Matsui, O., Sakamoto, M., Nakashima, O. et al. Management of hepatocellular carcinoma in Japan: Consensus-Based Clinical Practice Guidelines proposed by the Japan Society of Hepatology (JSH) 2010 updated version. Dig Dis. 2011;29(3):339-64.
14. Kyriakou, Y., Meyer, E., Prell, D. and Kachelriess, M. Empirical beam hardening correction (EBHC) for CT. Med Phys. 2010 Oct;37(10):5179-87.
15. Leng, S., Yu, L., Fletcher, J.G. and McCollough, C.H. Maximizing Iodine Contrast-to-Noise Ratios in Abdominal CT Imaging through Use of Energy Domain Noise Reduction and Virtual Monoenergetic Dual-Energy CT. Radiology. 2015 Aug;276(2):562-70.
16. Marin, D., Boll, D.T., Mileto, A. and Nelson, R.C. State of the art: dual-energy CT of the abdomen. Radiology. 2014 May;271(2):327-42.
17. Marin, D., Ramirez-Giraldo, J.C., Gupta, S., Fu, W., Stinnett, S.S., Mileto, A. et al. Effect of a Noise-Optimized Second-Generation Monoenergetic Algorithm on Image Noise and Conspicuity of Hypervascular Liver Tumors: An In Vitro and In Vivo Study. AJR Am J Roentgenol. 2016 Jun;206(6):1222-32.
18. Matsumoto, K., Jinzaki, M., Tanami, Y., Ueno, A., Yamada, M. and Kuribayashi, S. Virtual monochromatic spectral imaging with fast kilovoltage switching: improved image quality as compared with that obtained with conventional 120-kVp CT. Radiology. 2011 Apr;259(1):257-62.
19. Mileto, A., Nelson, R.C., Samei, E., Choudhury, K.R., Jaffe, T.A., Wilson, J.M. et al. Dual-energy MDCT in hypervascular liver tumors: effect of body size on selection of the optimal monochromatic energy level. AJR Am J Roentgenol. 2014 Dec;203(6):1257-64.
20. Schindera, S.T., Tock, I., Marin, D., Nelson, R.C., Raupach, R., Hagemeister, M. et al. Effect of beam hardening on arterial enhancement in thoracoabdominal CT angiography with increasing patient size: an in vitro and in vivo study. Radiology. 2010 Aug;256(2):528-35.
21. Shuman, W.P., Green, D.E., Busey, J.M., Kolokythas, O., Mitsumori, L.M., Koprowicz, K.M. et al. Model-based iterative reconstruction versus adaptive statistical iterative reconstruction and filtered back projection in liver 64-MDCT: focal lesion detection, lesion conspicuity, and image noise. AJR Am J Roentgenol. 2013 May;200(5):1071-6.
22. Shuman, W.P., Green, D.E., Busey, J.M., Mitsumori, L.M., Choi, E., Koprowicz,

K.M. et al. Dual-energy liver CT: effect of monochromatic imaging on lesion detection, conspicuity, and contrast-to-noise ratio of hypervascular lesions on late arterial phase. AJR Am J Roentgenol. 2014 Sep;203(3):601-6.

23. Yanaga, Y., Awai, K., Nakaura, T., Namimoto, T., Oda, S., Funama, Y. et al. Optimal contrast dose for depiction of hypervascular hepatocellular carcinoma at dynamic CT using 64-MDCT. AJR Am J Roentgenol. 2008 Apr;190(4):1003-9.

24. Young, S.W., Muller, H.H. and Marshall, W.H. Computed tomography: beam hardening and environmental density artifact. Radiology. 1983 Jul;148(1):279-83.

25. Yu, L., Leng, S. and McCollough, C.H. Dual-energy CT-based monochromatic imaging. AJR Am J Roentgenol. 2012 Nov;199(5 Suppl):S9-S15.

# Figure 1A

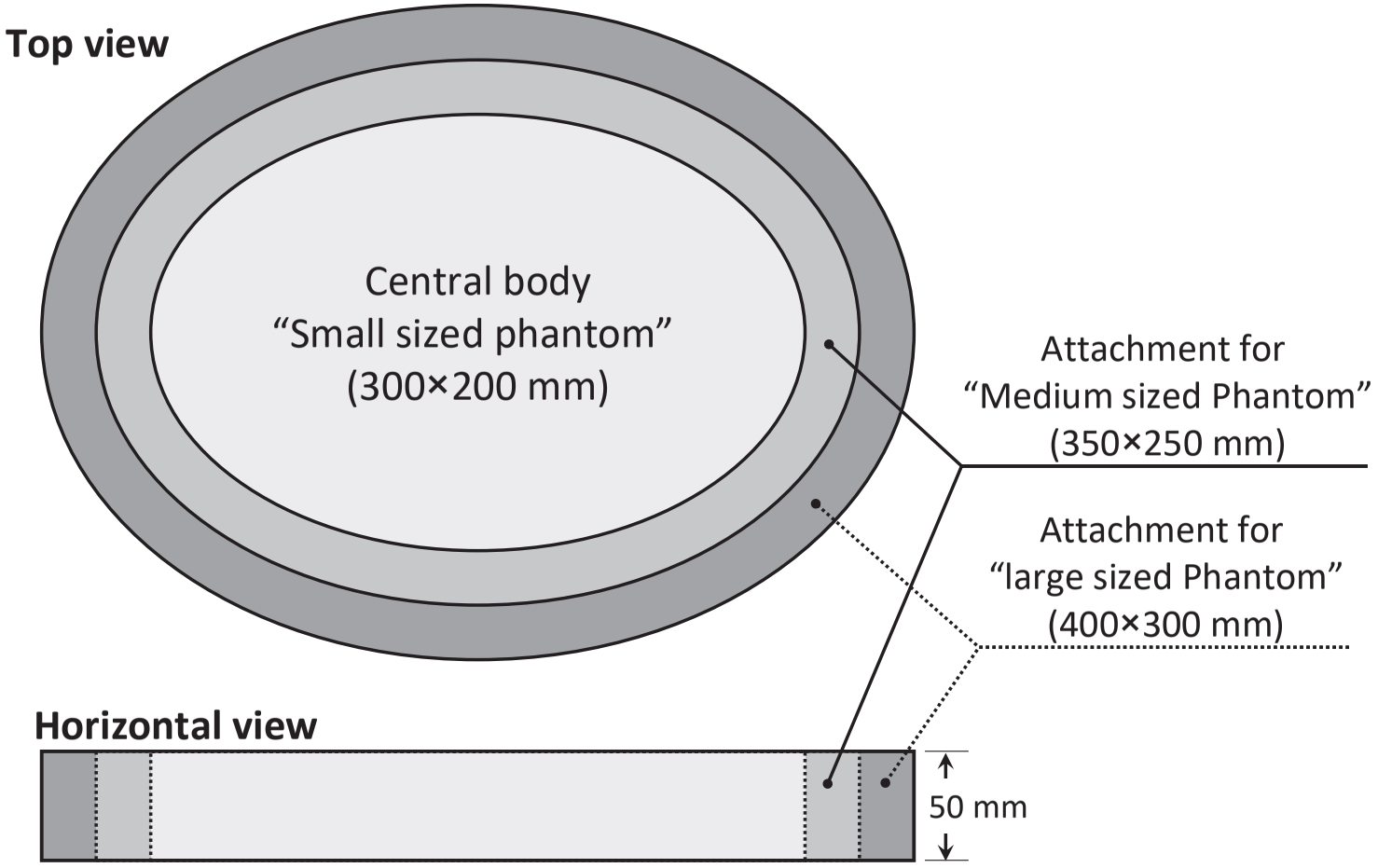
Top view
Central body
“Small sized phantom”
(300×200 mm)
Attachment for
“Medium sized Phantom”
(350×250 mm)
Attachment for
“large sized Phantom”
(400×300 mm)
Horizontal view
50 mm

# Figure 1B

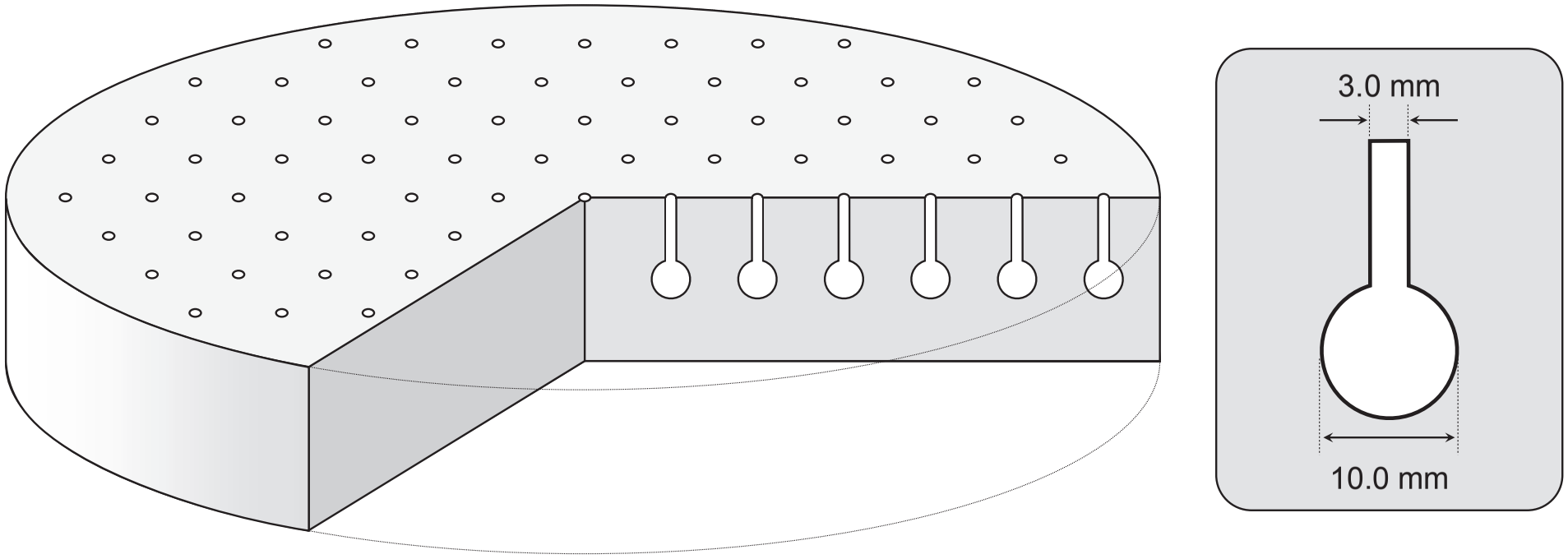

**Figure 1C**

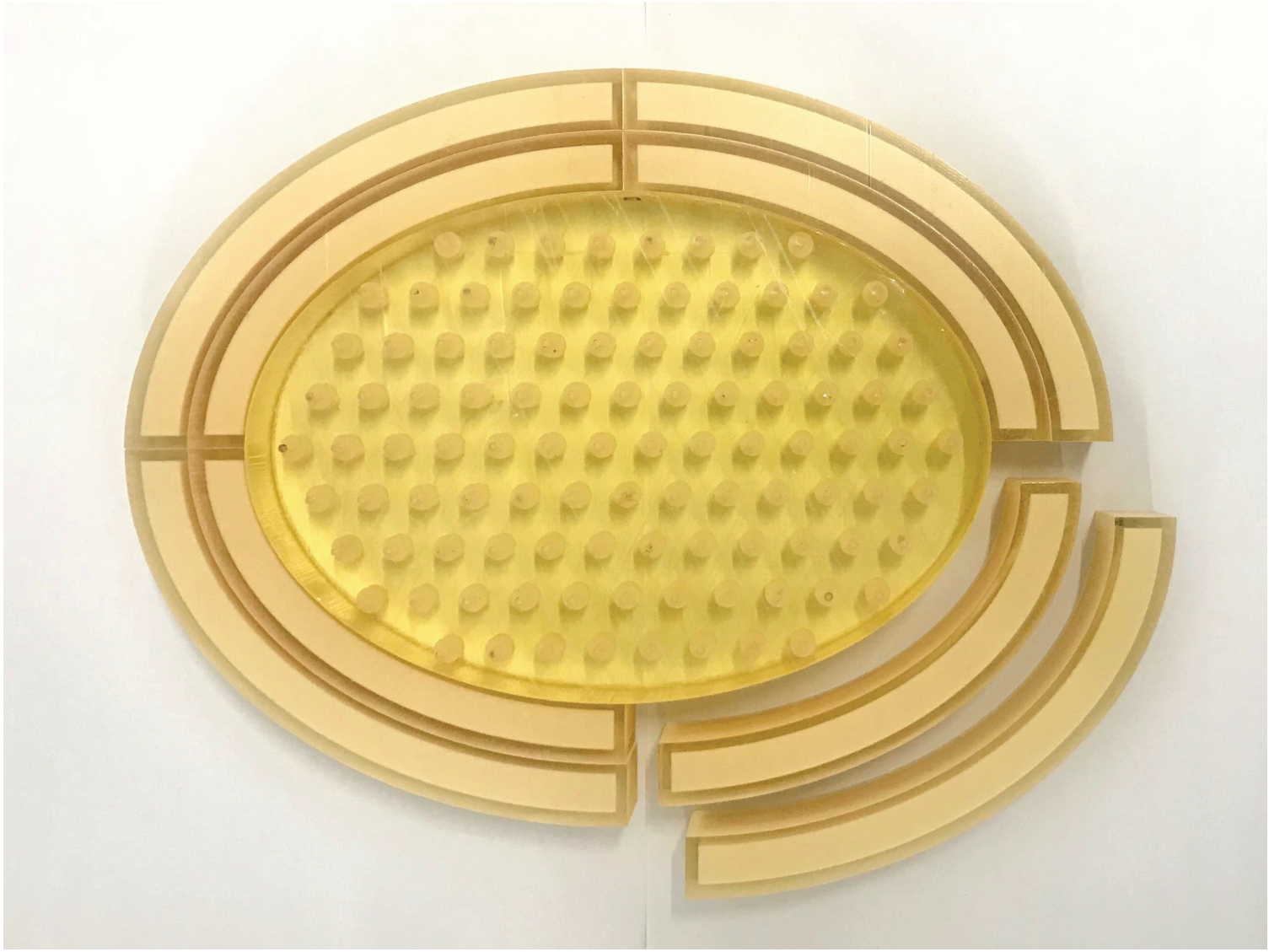

# Figure 2

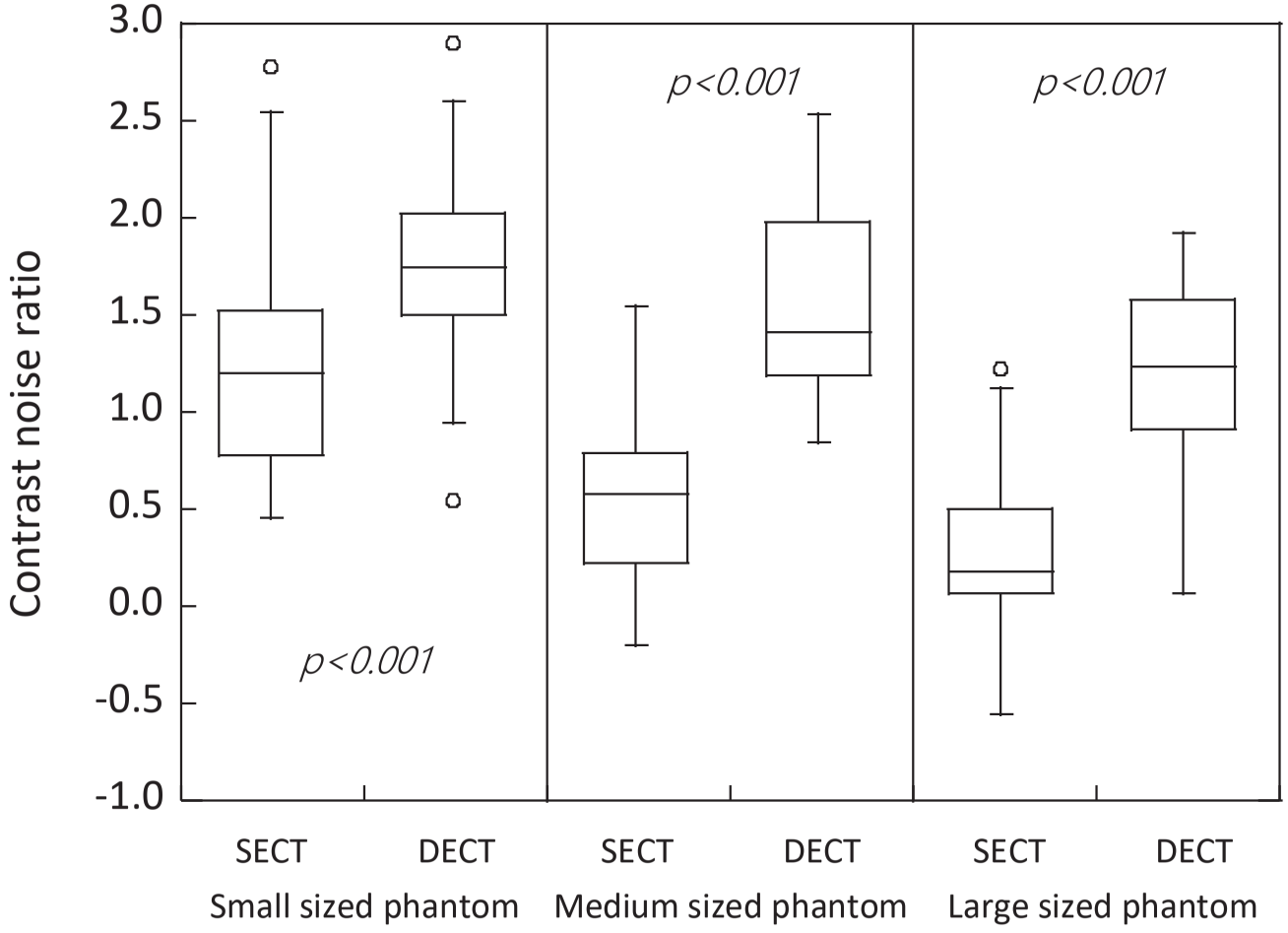
Contrast noise ratio
3.0
2.5
2.0
1.5
1.0
0.5
0.0
-0.5
-1.0
p<0.001
p<0.001
p<0.001
SECT
DECT
SECT
DECT
SECT
DECT
Small sized phantom
Medium sized phantom
Large sized phantom

# Figure 3A

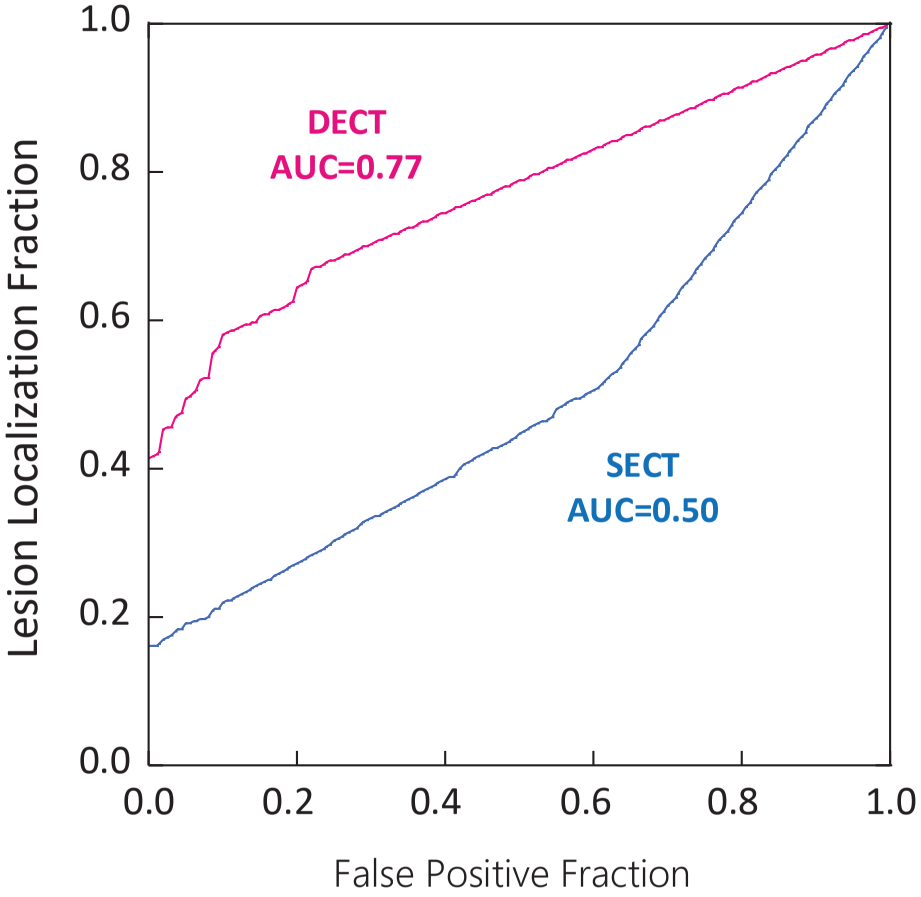
1.0
0.8
0.6
0.4
0.2
0.0
Lesion Localization Fraction
DECT
AUC=0.77
SECT
AUC=0.50
0.0
0.2
0.4
0.6
0.8
1.0
False Positive Fraction

# Figure 3B

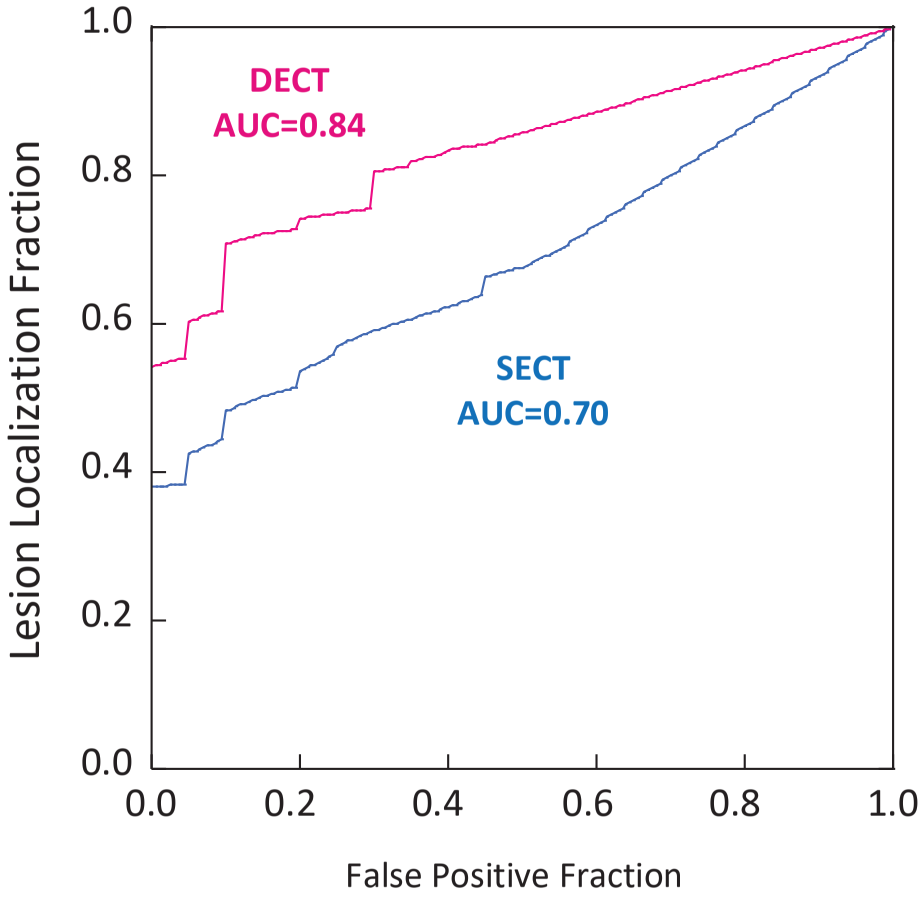
DECT
AUC=0.84
SECT
AUC=0.70
Lesion Localization Fraction
False Positive Fraction
0.0
0.2
0.4
0.6
0.8
1.0

# Figure 3C

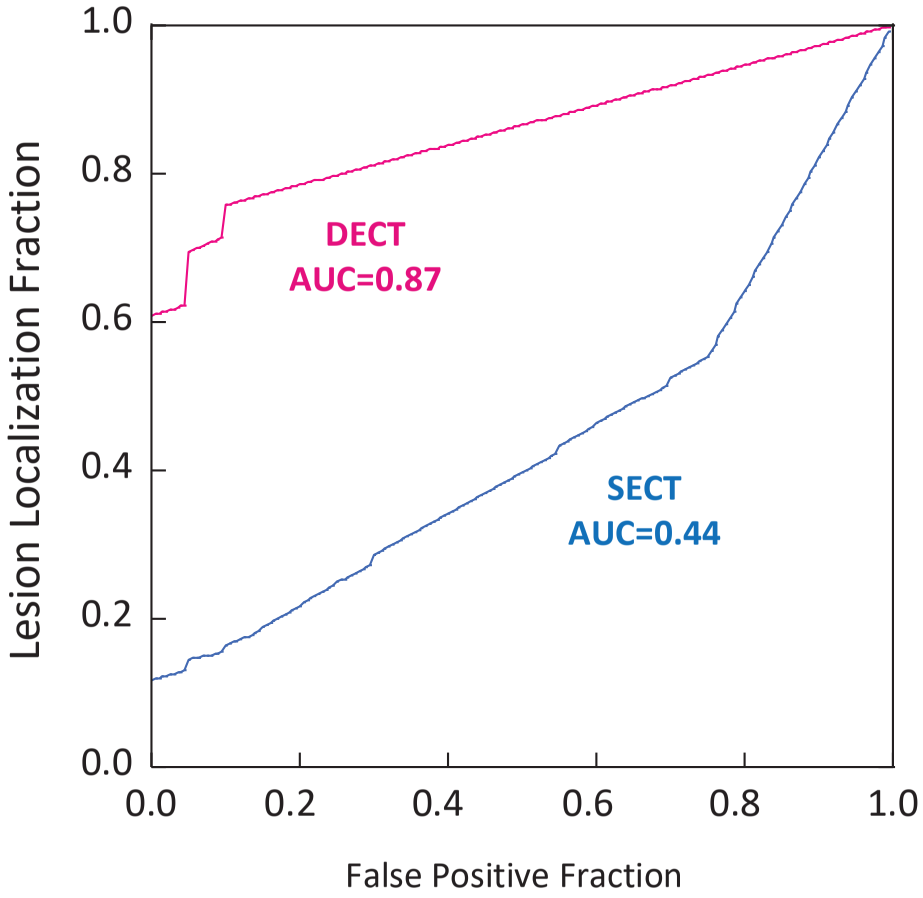
1.0
0.8
0.6
0.4
0.2
0.0
Lesion Localization Fraction
DECT
AUC=0.87
SECT
AUC=0.44
0.0
0.2
0.4
0.6
0.8
1.0
False Positive Fraction

# Figure 3D

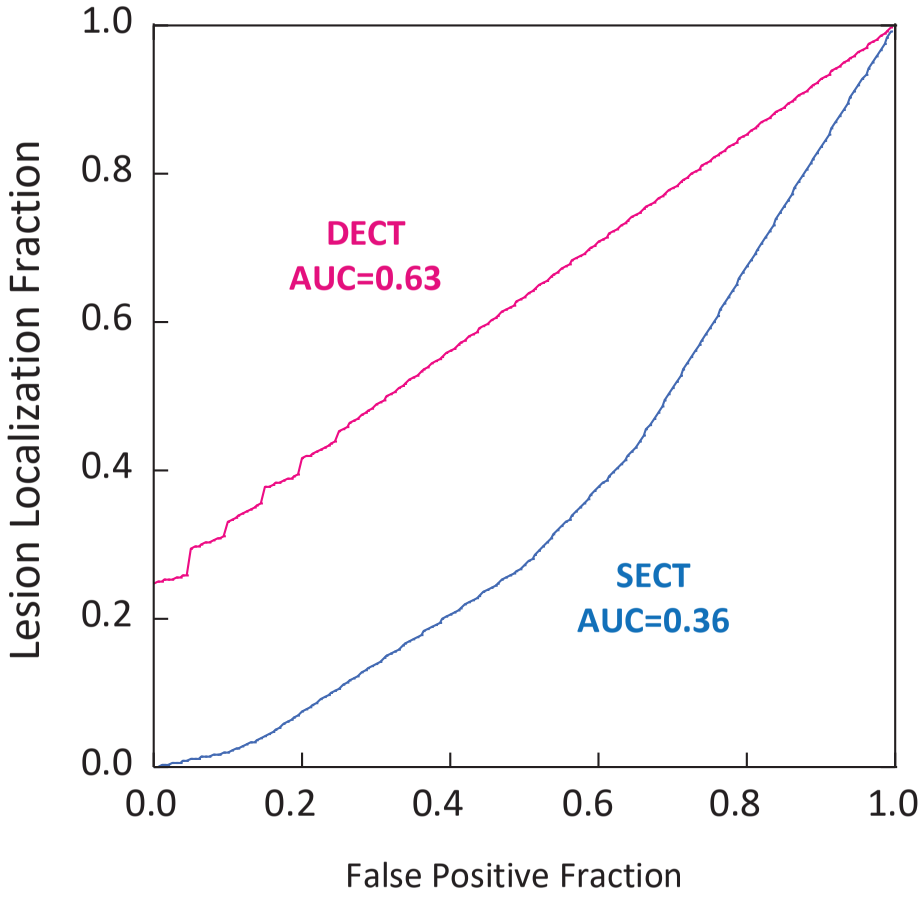
1.0
0.8
0.6
0.4
0.2
0.0
Lesion Localization Fraction
DECT
AUC=0.63
SECT
AUC=0.36
0.0
0.2
0.4
0.6
0.8
1.0
False Positive Fraction

Figure 4

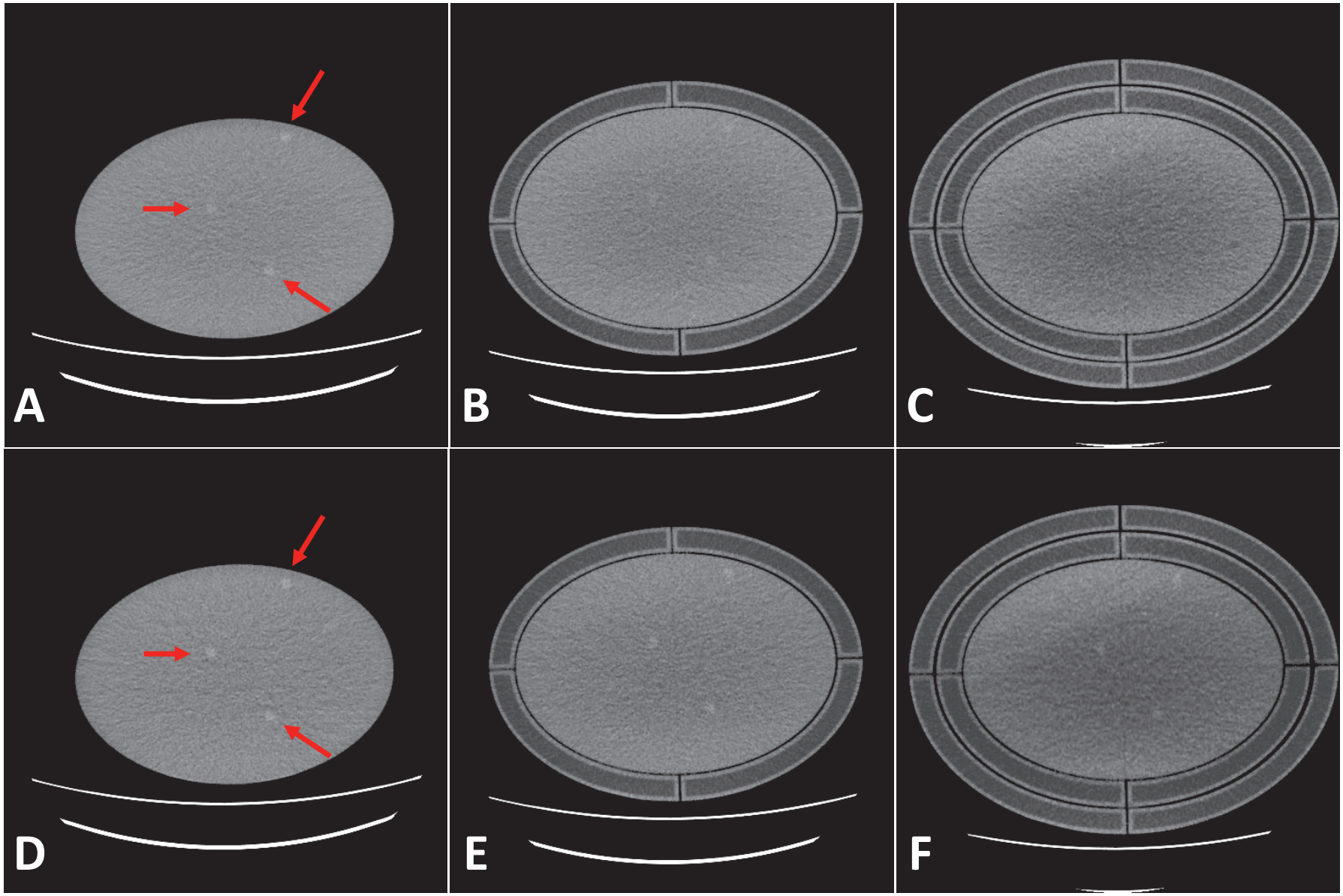

**Table 2. AUC values of each observer in the AFROC study**

| | AUC values | |
|---|---|---|
| Observer | SECT | DECT |
| 1 | 0.56 | 0.86 |
| 2 | 0.61 | 0.69 |
| 3 | 0.36 | 0.81 |
| 4 | 0.33 | 0.72 |
| 5 | 0.63 | 0.79 |
| Mean (SD) | 0.50 (0.14) | 0.77 (0.07) |